

Insights into the Impact of Impurities and Non-Stoichiometric Effects on the Electrochemical Performance of $\text{Li}_2\text{MnSiO}_4$

S. Fleischmann,^[a] M. Mancini,^{*[a]} P. Axmann,^[a] U. Golla-Schindler,^[b] U. Kaiser,^[b] and M. Wohlfahrt-Mehrens^[a]

A series of $\text{Li}_2\text{MnSiO}_4$ samples with various Li, Mn, and/or Si concentrations are reported to study for the first time the effect of impurities and deviation from ideal stoichiometry on electrochemical behavior. Carbon-coated and nanosized powders are obtained at 600 °C and compared with those synthesized at 900 °C. Samples are investigated using XRD, SEM, high-resolution TEM, attenuated total reflection infrared spectroscopy and Brunauer–Emmett–Teller surface area to characterize crystal structure, particle size, impurity amount, morphology, and surface area. Electrochemical performance depends on im-

purities such as MnO as well as crystallite size, surface area, and non-stoichiometric phases, which lead to the formation of additional polymorphs such as *Pmnb* and *P2₁/n* of $\text{Li}_2\text{MnSiO}_4$ at low calcination temperatures. A systematic analysis of the main parameters affecting the electrochemical behavior is performed and trends in synthesis are identified. The findings can be applied to optimize different synthesis routes for attaining stoichiometric and phase-pure *Pmn2₁* $\text{Li}_2\text{MnSiO}_4$ as cathode material for Li-ion batteries.

Introduction

The intensive search for high-capacity and high-energy lithium-ion-battery (LIB) cathode materials that are safe, inexpensive, and environmentally benign has led to the study of polyanion-type compounds of the orthosilicate family Li_2MSiO_4 ($M = \text{Fe}, \text{Mn}$).^[1,2] The high theoretical capacity of 333 mAh g^{-1} is based on the assumption of a reversible redox reaction with a two-electron transfer per formula unit. The theoretical voltage for redox steps $\text{Mn}^{2+/3+}$ and $\text{Mn}^{3+/4+}$ were calculated to be in the range of 4.1–4.5 V versus Li/Li^+ , favorable for high-energy cathode materials.^[3,4] The safety of these materials is related to the stable tetrahedral $[\text{SiO}_4]$ unit within the structure. Oxygen atoms are covalently bonded to silicon, hindering oxygen evolution and related events such as thermal runaway of the battery. The cost of the raw materials is less than those currently used for state-of-the-art cathodes, which include expensive metals such as cobalt. Importantly, the raw materials for orthosilicate cathodes, for example, silicon, iron, and/or manganese, are abundantly available in nature and nontoxic, which in turn further increases the safety of the battery.

Synthesis and characterization of $\text{Li}_2\text{MnSiO}_4$ as cathode material for LIBs were first demonstrated in 2006 by Dominko et al.^[2] Since this time, most studies utilizing common synthesis methods such as sol–gel, solid-state, and hydrothermal exhibit insufficient electrochemical performance with poor cycling stability, absence of expected voltage plateaus, and severe capacity fading after a few cycles.^[5] This has been attributed to the instability of the material during delithiation with a strong tendency to amorphize.^[3,4,6–8] The high reactivity of the active material towards HF, which is produced from the decomposition of standard electrolyte systems, further contributes to the reduction of the electrochemical performance.^[9] Few studies contradict these findings, and the synthesis procedures include, for example, the use of extremely high pressures or mesoporous carbons prepared by nanocasting.^[10–13] Regardless of the synthesis route applied, a common challenge of this material is to obtain a pure phase. Impurities such as MnO, Li_2SiO_3 , and Mn_2SiO_4 are often produced. Non-stoichiometry in the form of $\text{Li}_{2+2x}\text{Mn}_{1-x}\text{SiO}_4$ ($-1 \ll x < 1$) is possible due to solid solutions existing along the orthosilicate join.^[14] The complexity of the system is enhanced when considering the numerous possible polymorphs of $\text{Li}_2\text{MnSiO}_4$. The structure is related to the low (β) and high (γ) temperature forms of tetrahedral Li_3PO_4 - and Li_3PO_4 -derived structures, Li_2MXO_4 ($M = \text{Zn}^{2+}, \text{Mg}^{2+}$; $X = \text{Ge}^{4+}, \text{Si}^{4+}$) and consists of a distorted hexagonal closed packed oxygen array with Li, Mn, or Si atoms occupying half of the tetrahedral sites.^[15,16] The polymorphism is attributed to the orientation of the LiO_4 , MnO_4 , or SiO_4 tetrahedra, which could be pointing in the same or opposite directions or share corners and/or edges.^[16,17] Four polymorphs of $\text{Li}_2\text{MnSiO}_4$ have been reported, two 2D Li-layered orthorhombic forms, β_{II} -

[a] S. Fleischmann, Dr. M. Mancini, Dr. P. Axmann, Dr. M. Wohlfahrt-Mehrens
Accumulators Materials Research (ECM)
Zentrum für Sonnenenergie- und Wasserstoff-Forschung Baden-Württemberg (ZSW)

Helmholtzstr. 8, 89081 Ulm (Germany)
E-mail: marilena.mancini@zsw-bw.de

[b] Dr. U. Golla-Schindler, Prof. U. Kaiser
Electron Microscopy Group of Materials Science
Ulm University
Albert-Einstein-Allee 11, 89081 Ulm (Germany)

Supporting Information and the ORCID identification number(s) for the author(s) of this article can be found under <http://dx.doi.org/10.1002/cssc.201600894>.

$Pmn2_1$ and γ_{II} - $Pmnb$, and two 3D framework-structured monoclinic forms, γ_0 - $P2_1/n$ and Pn .^[2,14,18,19] Depending on the synthesis conditions, for example, the heat treatment applied, it is quite possible that a mixture of polymorphs is present due to their similar formation energies.^[16] In addition to mixed phases, intrinsic defects such as cation anti-site Li/Mn exchange may occur, which is expected to impede Li-ion pathways and effect rate capability of the material.^[17,20] The intrinsic conductivity of $\text{Li}_2\text{MnSiO}_4$ is also quite low, on the order of $10^{-16} \text{ S cm}^{-1}$ at room temperature, further contributing to the poor electrochemical performance.^[21]

Reports of $\text{Li}_2\text{MnSiO}_4$ clearly support irreversible structural change as the main cause for rapid capacity fading; however, the influence of by-products, often reported solely as unavoidable, and non-stoichiometric phases of $\text{Li}_2\text{MnSiO}_4$ on the overall electrochemical performance are generally not discussed and to the best of our knowledge have not been investigated.^[22] In this work, the stoichiometry of the reactants is systematically varied during synthesis to obtain samples with controlled amounts of by-products in addition to the active phase with the ideal composition of $\text{Li}_2\text{MnSiO}_4$. The influence of sample composition, non-stoichiometry, and physical properties such as particle size and surface area on the electrochemical performance of $\text{Li}_2\text{MnSiO}_4$ is investigated.

Results and Discussion

Phase and structural analysis

For the purpose of this study, the composition of the synthesized powders has been estimated based upon the phase compatibility diagram of the Li_2O – MnO – SiO_2 system shown in Figure 1. The red points within the phase diagram indicate the specific Li/Mn/Si atomic ratio of the investigated samples. Sample names and estimated final composition present at equilibrium conditions are reported in Table 1. The $\text{Li}_2\text{MnSiO}_4$

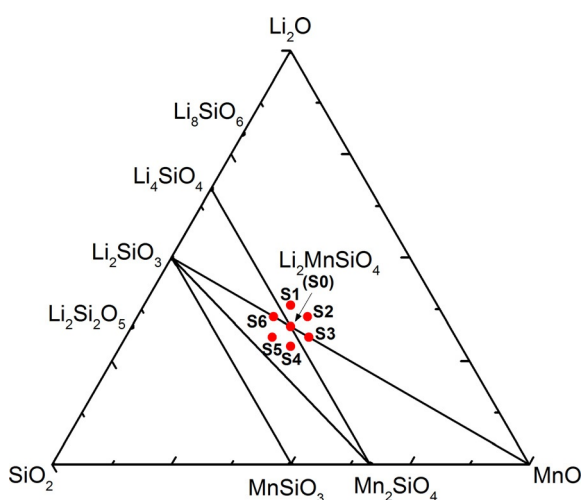


Figure 1. Phase compatibility diagram of the Li_2O – MnO – SiO_2 system at 950–1050 °C adapted from Ref. [14]. Compositions of synthesized samples are shown as points S0–S6.

Table 1. Estimated compositions of the synthesized samples S0–S6.

Sample	Molar ratio Li/Mn/Si	Molar excess	Experimental composition [mol] ([wt %])
S0	2:1:1	none	1 $\text{Li}_2\text{MnSiO}_4$ (100% $\text{Li}_2\text{MnSiO}_4$)
S1	2.5:1:1	Li	1 $\text{Li}_{2+2x}\text{Mn}_{1-x}\text{SiO}_4 + 0.25 \text{ MnO}$, $x = 0.25$ (89% $\text{Li}_{2+2x}\text{Mn}_{1-x}\text{SiO}_4 + 11\% \text{ MnO}$)
S2	2.5:1.25:1	Li, Mn	1 $\text{Li}_{2+2x}\text{Mn}_{1-x}\text{SiO}_4 + 0.5 \text{ MnO}$, $x = 0.25$ (81% $\text{Li}_{2+2x}\text{Mn}_{1-x}\text{SiO}_4 + 19\% \text{ MnO}$)
S3	2:1.25:1	Mn	1 $\text{Li}_2\text{MnSiO}_4 + 0.25 \text{ MnO}$ (90% $\text{Li}_2\text{MnSiO}_4 + 10\% \text{ MnO}$)
S4	2:1.25:1.25	Mn, Si	0.75 $\text{Li}_2\text{MnSiO}_4 + 0.25 \text{ Li}_2\text{SiO}_3 + 0.25 \text{ Mn}_2\text{SiO}_4$ (62% $\text{Li}_2\text{MnSiO}_4 + 12\% \text{ Li}_2\text{SiO}_3 + 26\% \text{ Mn}_2\text{SiO}_4$)
S5	2:1:1.25	Si	0.5 $\text{Li}_2\text{MnSiO}_4 + 0.5 \text{ Li}_2\text{SiO}_3 + 0.25 \text{ Mn}_2\text{SiO}_4$ (46% $\text{Li}_2\text{MnSiO}_4 + 26\% \text{ Li}_2\text{SiO}_3 + 29\% \text{ Mn}_2\text{SiO}_4$)
S6	2.5:1:1.25	Li, Si	1 $\text{Li}_2\text{MnSiO}_4 + 0.25 \text{ Li}_2\text{SiO}_3$ (88% $\text{Li}_2\text{MnSiO}_4 + 12\% \text{ Li}_2\text{SiO}_3$)

samples were prepared using a common synthesis technique of solid-state reaction.^[22] The stoichiometry of the reactants was systematically varied to obtain samples with controlled amounts of frequently reported by-products in addition to the active phase with the ideal composition of $\text{Li}_2\text{MnSiO}_4$. Each sample composition can be estimated according to the ratio of the reactants used for the synthesis. Sample S0 is expected to have ideal composition for which the Li/Mn/Si atomic ratio is 2:1:1. Each sample from S1 to S6 contains an excess of one or two elements as shown in Table 1. The aim was to identify the phases and relative amounts formed during synthesis and to investigate their effect on $\text{Li}_2\text{MnSiO}_4$ properties.

The reference phase diagram in Figure 1 was obtained for 950–1050 °C; therefore, in the present study the samples were calcined at 900 °C to allow direct comparison.^[14] At this temperature, however, it is difficult to obtain small $\text{Li}_2\text{MnSiO}_4$ crystals of which the size increases with increasing calcination temperature. Due to the inherently low conductivity of $\text{Li}_2\text{MnSiO}_4$, nanosized crystals and in situ conductive coatings such as carbon are necessary to overcome the kinetic limitations of the material and permit suitable electrochemical behavior. As observed for LiFePO_4 , for example, nanosized particles with conductive coatings reduce the mean free path of the electrons and promote fast interfacial ionic charge transfer, thereby improving the kinetics of the material.^[23–25] With the aim of obtaining nanosized $\text{Li}_2\text{MnSiO}_4$ samples suitable for electrochemical investigation, all compositions were also synthesized at 600 °C and the structural results compared with those calcined at 900 °C.

XRD analysis of all samples was performed and the diffractograms are shown in Figure 2. The samples calcined at 900 °C (Figure 2a) show higher crystallinity than those at 600 °C (Figure 2b), indicated by the sharper diffraction peaks in the diffractograms. The synthesis conditions allow carbon-coated particles to be obtained due to the decomposition of the organic part of the precursors.^[22] The carbon amount is approximately 5 wt% for all synthesized compounds, as determined by elemental analysis. XRD analysis shows no clear peaks corresponding to carbon, indicating an amorphous nature of the

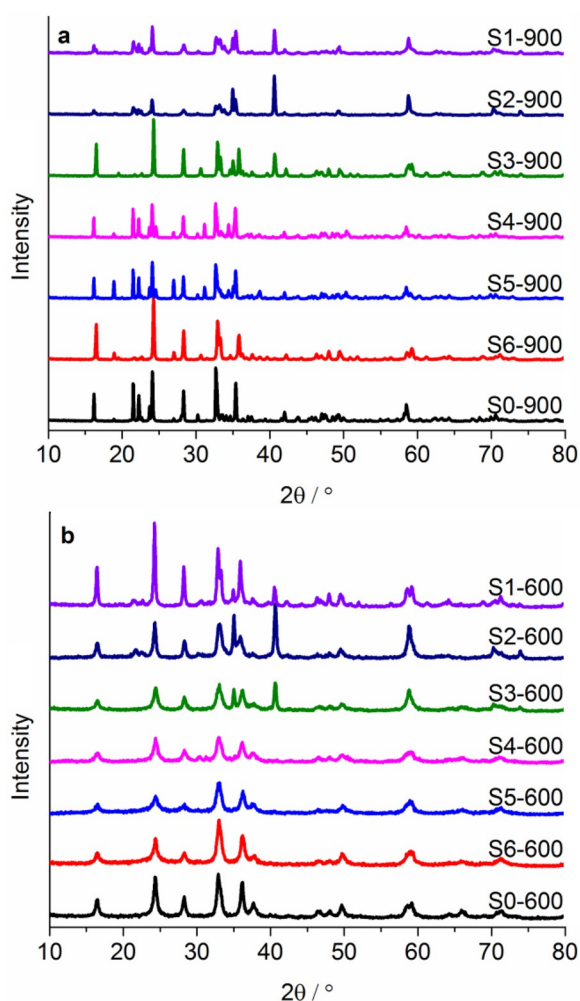


Figure 2. XRD patterns of samples containing varying Li/Mn/Si stoichiometry as listed in Table 1, synthesized at a) 900 and b) 600 °C.

carbon coating. We performed Rietveld analysis for all samples to determine the $\text{Li}_2\text{MnSiO}_4$ crystal structure, crystal size, lattice parameters, and amount of crystalline by-products. Structural models of the $\text{Li}_2\text{MnSiO}_4$ polymorphs $\beta_{\text{II}}\text{-Pmnb}$, $\gamma_{\text{II}}\text{-Pmnb}$, and $\gamma_0\text{-P2}_1/n$ reported in literature were applied.^[2,14,18] The results are summarized in Table 2 along with the agreement indices, which are an indication for the quality of the refinement. For all samples, the main reflections in Figure 2a were indexed to the typical high-temperature forms of $\text{Li}_2\text{MnSiO}_4$, namely the $\gamma_0\text{-P2}_1/n$ monoclinic (PDF 00-055-0704) or $\gamma_{\text{II}}\text{-Pmnb}$ orthorhombic (PDF 01-080-8499) polymorphs. Most samples obtained at 900 °C crystallize as the $\gamma_0\text{-P2}_1/n$ polymorph although this structure has been reported to form by quenching the material after high-temperature treatment, that is > 900 °C.^[16,26] This result is thus unexpected as our samples are slowly cooled from 900 °C to room temperature. Only samples S3-900 and S6-900 could be indexed solely to the $\gamma_{\text{II}}\text{-Pmnb}$ polymorph. The formation of the $\gamma_0\text{-P2}_1/n$ polymorph of $\text{Li}_2\text{MnSiO}_4$ may, therefore, depend on the overall composition of the sample, that is, the presence of different by-products as listed in Table 2. XRD

profiles and Rietveld refinement results of selected samples are shown in Figure 3. Refinement results of all samples can be found in the Supporting Information.

Sample S0-900 (Figure 3a), with a Li/Mn/Si atomic ratio of 2:1:1, is indexed to the $\gamma_0\text{-P2}_1/n$ polymorph of $\text{Li}_2\text{MnSiO}_4$. This sample contains Li_2SiO_3 (PDF 01-070-0330) as impurity at approximately 3 wt% as determined from XRD measurements. Samples S1-900 and S2-900 are the only samples containing a mixture of $\text{Li}_2\text{MnSiO}_4$ polymorphs, $\text{P2}_1/n$ and Pmnb . The Rietveld fits are shown in Figure 3b and c. A mixture of polymorphs in these samples could be attributed to their similar formation energies; however, this would not explain the reason why it is not observed for the other samples.^[16] The presence of two polymorphs can possibly be understood by considering the composition of the samples, which is located within the region $\text{Li}_2\text{O-Li}_4\text{SiO}_4\text{-Li}_2\text{MnSiO}_4\text{-MnO}$ of the phase diagram. Along the $\text{Li}_4\text{SiO}_4\text{-Li}_2\text{MnSiO}_4$ segment, solid solutions of the composition $\text{Li}_{2+2x}\text{Mn}_{1-x}\text{SiO}_4$ ($0 \leq x \leq 0.2$) were reported.^[14] For similar structures, that is, Li_3PO_4 -type or LISICON (lithium super ionic conductor) structures, for example, $\text{Li}_2\text{MgSiO}_4$, $\text{Li}_2\text{ZnSiO}_4$, and $\text{Li}_2\text{ZnGeO}_4$, extensive solid solutions along the orthosilicate join $\text{Li}_4\text{XO}_4\text{-M}_2\text{XO}_4$ ($\text{M} = \text{Mg}^{2+}, \text{Zn}^{2+}; \text{X} = \text{Si}^{4+}, \text{Ge}^{4+}$) are commonly observed.^[15,27,28] Interesting to note is the complexity of such joins and the numerous phases and binary phases that can be present depending on the stoichiometry and the heat treatment applied. Accordingly, both samples S1-900 and S2-900 are expected to contain Li-rich solid solutions of composition $\text{Li}_{2+2x}\text{Mn}_{1-x}\text{SiO}_4$ ($0 < x < 1$).

As observed for $\text{Li}_{2+2x}\text{Zn}_{1-x}\text{SiO}_4$ ($-1 < x < 1$) solid solutions, two-phases ($\beta + \gamma$) form when the Li amount exceeds a certain value.^[27] The β phase has a composition close to the ideal Li/Zn cation ratio of 2:1 and exhibits a limited range of solid solutions, $\text{Li}_{2+2x}\text{Zn}_{1-x}\text{SiO}_4$ where $-0.02 < x < 0.18$. As the Li content exceeds this amount, a Li-rich γ -phase forms additionally to the β -phase. Since samples S1-900 and S2-900 contain a high amount of excess Li, that is, $x = 0.25$, we can assume that a binary phase is likely to form. Based on the refinement results, a binary phase ($\beta + \gamma$) is indeed observed. The β phase has an orthorhombic structure of space group Pmnb with a calculated Li/Mn ratio of 2.02:0.98 and 2.06:0.94 for samples S1-900 and S2-900, respectively. The Li-rich γ phase with $\text{P2}_1/n$ monoclinic structure has a calculated Li/Mn ratio of 2.19:0.81 and 2.18:0.82, respectively. It is worth noting, however, that the applied models do not take into account Li atoms that could occupy unknown coordination sites within the structure to maintain the charge balance. Due to the aliovalent substitution of Li atoms for Mn ions in $\text{Li}_2\text{MnSiO}_4$, a charge compensation mechanism is required to maintain charge neutrality of the compound. Charge compensation may occur by either Li interstitials or a change in oxidation state of Mn. Due to the slightly reductive calcination conditions applied during synthesis, a change in oxidation state of Mn is not likely to occur. Therefore, Li interstitials within the structure are expected. It is possible that the Li atoms would be placed similarly to those in the Li_4SiO_4 structure, where Li atoms additionally occupy sites of 5- and 6-fold coordination.^[29] For every 2 mol of Li re-

Table 2. Results of XRD analysis of samples S0–S6 calcined at 900 and 600 °C. Detected crystalline phases, crystal size, lattice parameters, and agreement indices are shown. Errors are shown in parenthesis.

Sample	900 °C				600 °C			
	detected crystalline phases	crystal size [nm]	Li ₂ MnSiO ₄ lattice parameters [Å]	R _{wp} /χ ^{2(a)}	detected crystalline phases	crystal size [nm]	Li ₂ MnSiO ₄ lattice parameters [Å]	R _{wp} /χ ^{2(a)}
S0	97.49(0.22) % Li ₂ MnSiO ₄ P2 ₁ /n 2.51(0.22) % Li ₂ SiO ₃	193(11)	a = 6.33735(43) b = 10.90675(73) c = 5.07540(30) β = 91.0156(31)	16.82/1.22	100 % Li ₂ MnSiO ₄ Pmn2 ₁	7.56(0.28)	a = 6.307(12) b = 5.394(11) c = 4.9726(94)	14.50/1.25
S1	53.8(3.0) % Li ₂ MnSiO ₄ P2 ₁ /n 26.7(1.9) % Li ₂ MnSiO ₄ Pmnb 13.34(0.88) % MnO 4.59(0.91) % Li ₄ SiO ₄ 0.53(0.12) % SiO ₂ quartz 0.99(0.13) % SiO ₂ tridymite	61.8(4.9) > 250	P2 ₁ /n: a = 6.33461(73) b = 10.8714(15) c = 5.07315(71) β = 91.009(11) Pmnb: a = 6.2341(21) b = 10.7626(29) c = 5.0666(15)	18.81/1.39	31.9(1.4) % Li ₂ MnSiO ₄ Pmn2 ₁ 63.0(1.4) % Li ₂ MnSiO ₄ Pmnb 5.1(0.24) % MnO	28.4(2.8) 23.0(2.1)	Pmn2 ₁ : a = 6.3187(12) b = 5.3858(11) c = 5.0036(11) Pmnb: a = 6.3169(22) b = 10.7924(37) c = 5.0066(13)	18.42/1.46
S2	39.7(4.6) % Li ₂ MnSiO ₄ P2 ₁ /n 27.7(2.4) % Li ₂ MnSiO ₄ Pmnb 27.4(2.1) % MnO 3.7(1.1) % Li ₄ SiO ₄ 0.43(0.16) % SiO ₂ quartz 1.14(0.19) % SiO ₂ tridymite	56.5(6.7) > 250	P2 ₁ /n: a = 6.3434(12) b = 10.8770(24) c = 5.0778(12) β = 90.975(17) Pmnb: a = 6.2402(27) b = 10.7714(38) c = 5.0734(20)	20.98/1.45	13.9(1.9) % Li ₂ MnSiO ₄ Pmn2 ₁ 71.6(3.0) % Li ₂ MnSiO ₄ P2 ₁ /n 14.5(1.4) % MnO	25.1(2.2) 14.4(1.3)	Pmn2 ₁ : a = 6.3067(15) b = 5.3835(15) c = 5.0032(20) P2 ₁ /n: a = 6.2584(48) b = 10.8229(99) c = 5.0189(19) β = 90.59(11)	14.95/1.19
S3	86.63(0.22) % Li ₂ MnSiO ₄ Pmnb 13.37(0.22) % MnO	92.0(3.7)	a = 6.30672(69) b = 10.7626(12) c = 5.01470(59)	16.89/1.22	90.43(0.23) % Li ₂ MnSiO ₄ Pmn2 ₁ 9.57(0.23) % MnO	9.31(0.22)	a = 6.3114(40) b = 5.3896(38) c = 4.9755(32)	15.25/1.09
S4	72.2(1.1) % Li ₂ MnSiO ₄ P2 ₁ /n 5.66(0.32) % Li ₂ SiO ₃ 22.11(0.85) % Mn ₂ SiO ₄	182(14)	a = 6.34003(56) b = 10.90566(93) c = 5.07601(39) β = 91.0072(40)	16.83/1.19	93.51(0.64) % Li ₂ MnSiO ₄ Pmn2 ₁ 0 % Li ₂ SiO ₃ 2.98(0.29) % Mn ₂ SiO ₄ 3.51(0.59) % MnSiO ₃	8.60(0.16)	a = 6.3156(38) b = 5.3999(37) c = 4.9781(31)	15.03/1.09
S5	62.0(1.2) % Li ₂ MnSiO ₄ P2 ₁ /n 19.26(0.66) % Li ₂ SiO ₃ 18.69(0.64) % Mn ₂ SiO ₄	246(24)	a = 6.33927(46) b = 10.90823(81) c = 5.07548(35) β = 91.0190(37)	15.36/1.14	100 % Li ₂ MnSiO ₄ Pmn2 ₁ 0 % Li ₂ SiO ₃ 0.32(0.34) % Mn ₂ SiO ₄	7.91(0.18)	a = 6.305(13) b = 5.407(12) c = 4.962(10)	15.62/1.21
S6	89.8(0.35) % Li ₂ MnSiO ₄ Pmnb 10.2(0.35) % Li ₂ SiO ₃	79.8(3.7)	a = 6.30262(95) b = 10.7662(18) c = 5.01591(75)	18.56/1.40	100 % Li ₂ MnSiO ₄ Pmn2 ₁ 0 % Li ₂ SiO ₃	9.97(0.24)	a = 6.3017(92) b = 5.3951(84) c = 4.9659(73)	14.83/1.23

[a] R_{wp} = residual weighted pattern, χ² = goodness of fit.

placed in Li₂MnSiO₄, 1 mol of Mn must leave the structure to maintain the charge balance.

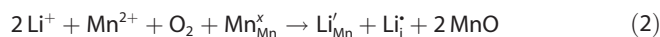
This is represented using the Kröger–Vink notation as following:



The Mn not consumed in forming Li_{2+2x}Mn_{1-x}SiO₄ (0 < x < 1) would result in MnO as by-product.

In the case where both Li and Mn are present in excess, as is the case for sample S2, a Li-rich Li_{2+2x}Mn_{1-x}SiO₄ (0 < x < 1) phase can result. Due to the composition of sample S2, that is, location on the Li₂O–MnO–SiO₂ phase diagram, it can be expected that excess Mn will not enter into the Li_{2+2x}Mn_{1-x}SiO₄

(0 < x < 1) structure but rather be converted into an additional amount of MnO secondary phase:



This reaction can explain the amount of MnO (PDF 01-076-9117) in samples S1-900 and S2-900. Sample S2-900 contains approximately twice the amount of MnO as sample S1-900, with values of approximately 27 and 13 wt %, respectively.

Besides the (β + γ) Li_{2+2x}Mn_{1-x}SiO₄ (0 < x < 1) and MnO phases, very small amounts of three additional crystalline phases, Li₄SiO₄ (PDF 01-074-0307), β-quartz (PDF 01-081-1655), and β-tridymite (PDF 01-089-3608), could be identified from

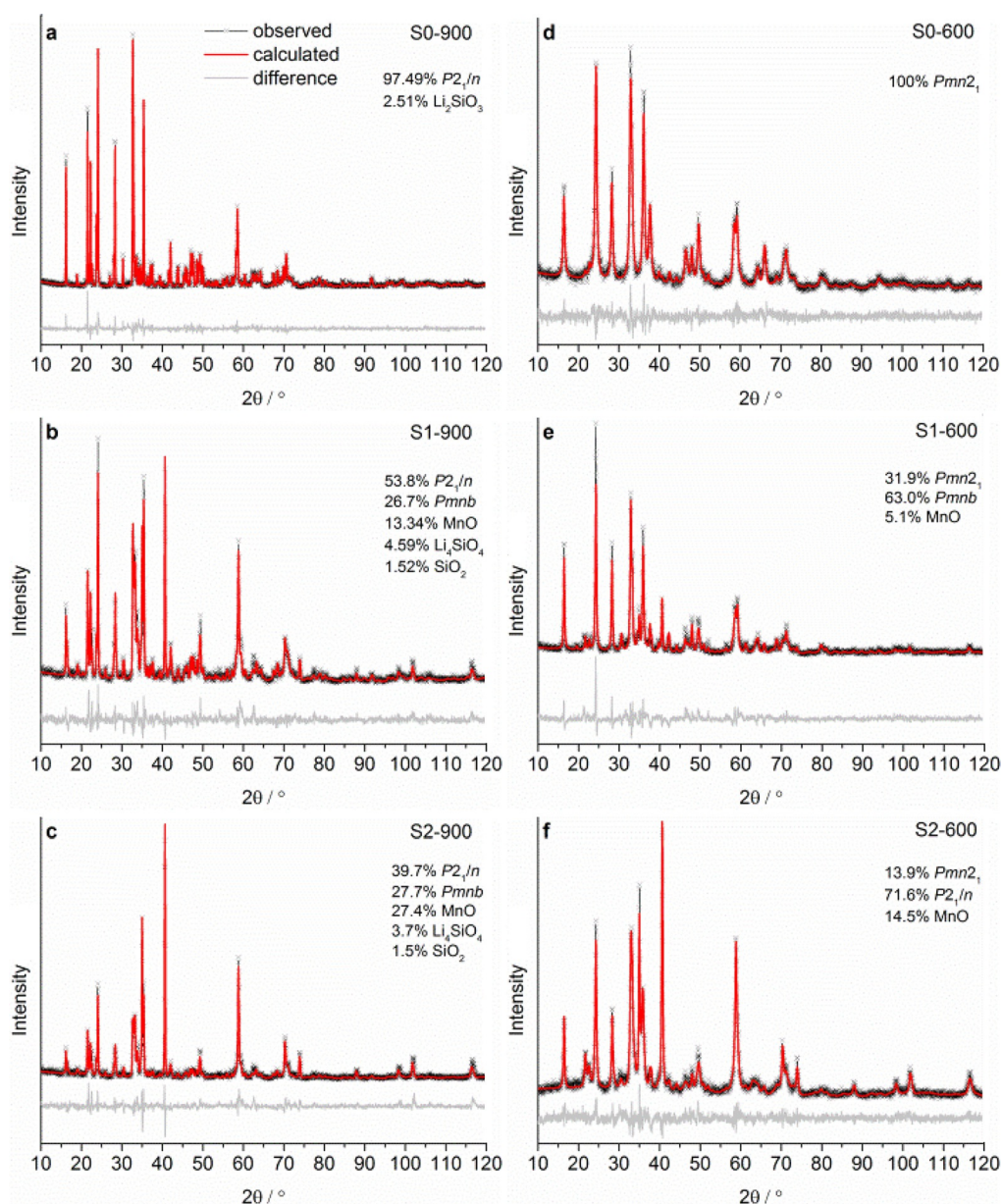


Figure 3. Rietveld refinement of $\text{Li}_2\text{MnSiO}_4$ samples a) S0-900, b) S1-900, c) S2-900, d) S0-600, e) S1-600, and f) S2-600. The observed pattern is shown as dots, calculated and fitted patterns as solid lines.

the refinement. The formation of these phases is not thermodynamically favored, but their presence is possible due to inhomogeneous mixing of the reactants or non-equilibrium conditions.

The composition of sample S3-900 is located on the $\text{Li}_2\text{MnSiO}_4$ -MnO tie line of the phase diagram where only the two aforementioned phases are expected. In the XRD patterns, the γ_{II} - $Pmnb$ polymorph of $\text{Li}_2\text{MnSiO}_4$ can be detected along with approximately 13 wt% MnO secondary phase as calculated from the refinement. The amount of MnO is approximately equal to the amount in sample S1-900 as estimated from the phase diagram. The MnO amounts for samples S1-900, S2-900, and S3-900 are higher than predicted. The estimated values and results are shown in Table 1 and Table 2 respectively.

The composition of samples S4-900 and S5-900 lies within the triangle Li_2SiO_3 - $\text{Li}_2\text{MnSiO}_4$ - Mn_2SiO_4 in the phase diagram, where all three phases are expected to be present. These compositions were chosen to obtain samples that contain two commonly reported impurities, Li_2SiO_3 and Mn_2SiO_4 . These secondary phases are thermodynamically favored when excess Si is present during the synthesis of $\text{Li}_2\text{MnSiO}_4$. The Li_2SiO_3 - $\text{Li}_2\text{MnSiO}_4$ - Mn_2SiO_4 triangle includes the Mn-rich segment of the orthosilicate tie line $\text{Li}_2\text{MnSiO}_4$ - Mn_2SiO_4 . As discussed previously for similar orthosilicate systems, for example, Li_4SiO_4 - Zn_2SiO_4 , the maximum amount of Zn present in solid solution is quite low, that is, $x=0.02$. A Zn-rich solid solution is therefore not favored but instead the formation of Zn_2SiO_4 . Accordingly, it is unlikely in the Li_4SiO_4 - Mn_2SiO_4 orthosilicate system

that a Mn-rich $\text{Li}_{2-2x}\text{Mn}_{1+x}\text{SiO}_4$ phase will appear but rather the Mn_2SiO_4 impurity.

In agreement with the phase diagram, both crystalline phases Li_2SiO_3 and Mn_2SiO_4 (PDF 01-074-0716) were detected in samples S4-900 and S5-900 using XRD, as shown in Table 2. The $\text{Li}_2\text{MnSiO}_4$ phase in samples S4-900 and S5-900 crystallizes as the γ_0 - $P2_1/n$ polymorph with calculated Li/Mn cation ratios of 2.05:0.95 and 2.06:0.94, respectively. This ratio is near the stoichiometric Li/Mn cation ratio of 2:1, indicating that a Mn-rich phase did not form as expected.

The composition of sample S6-900 lies along the Li_2SiO_3 – $\text{Li}_2\text{MnSiO}_4$ tie line in the phase diagram; therefore, only these two phases are predicted to be present. The XRD analysis shows that sample S6-900 crystallizes as the expected γ_{II} - $Pmnb$ polymorph of $\text{Li}_2\text{MnSiO}_4$. The sample contains 10 wt% of Li_2SiO_3 as by-product, which corresponds approximately to the estimated amount for this sample as shown in Table 1.

As previously mentioned, the large crystal size of the samples calcined at 900 °C is expected to result in poor electrochemical performance. Additionally, the range of crystal size is quite broad between samples. This alone hinders the ability to differentiate the effects on electrochemical behavior based solely on the material composition. It is therefore necessary to carry out the synthesis applying a lower calcination temperature to produce nanocrystalline powders. The diffractograms of the samples calcined at 600 °C are reported in Figure 2b. Compared to the samples calcined at 900 °C shown in Figure 2a, they show broader peaks and lower signal/noise ratios, indicating relatively low crystallinity and small crystallite size.

Selected SEM micrographs of the synthesized samples are shown in Figure 4. Sample S0 calcined at 600 °C (Figure 4a) consists of an agglomeration of nanosized crystallites. Sample S1-600 (Figure 4b) containing excess Li has the appearance of more closely packed nanosized crystallites than sample S0-600. The morphology changes when calcined at the higher temperature (900 °C) and consists of larger particles and plate-like aggregates (Figure 4c and d).

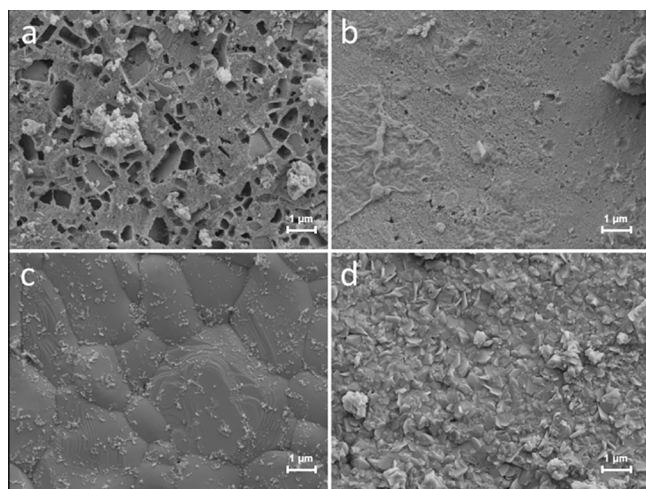


Figure 4. SEM micrographs of selected synthesized samples: (a) S0-600, (b) S1-600, (c) S0-900, and (d) S1-900.

All samples obtained at 600 °C show typical reflections of the low-temperature orthorhombic form of $\text{Li}_2\text{MnSiO}_4$.^[2] Indeed, for these samples the crystal size shown in Table 2 is much smaller than for the samples prepared at 900 °C. Rietveld fits of a few chosen compositions calcined at 600 °C are shown in Figure 3.

Sample S0-600 (Figure 3d) with a composition Li/Mn/Si of 2:1:1 is indexed to the β_{II} - $Pmn2_1$ polymorph of $\text{Li}_2\text{MnSiO}_4$ (PDF 01-075-7861). No secondary crystalline phases are identified by XRD, indicating a pure $\text{Li}_2\text{MnSiO}_4$ phase. This result however differs to that of sample S0-900 where a small amount of crystalline Li_2SiO_3 was detected.

The patterns of samples S1-600 (Figure 3e) and S2-600 (Figure 3f) can be partially fitted to the β_{II} - $Pmn2_1$ polymorph of $\text{Li}_2\text{MnSiO}_4$. Observed peaks at 2θ angles 21.6° (110) and 22.7° (101) are ascribed to the β_{II} - $Pmn2_1$ polymorph but are only observed for these two samples.^[2,26] Moreover, the diffractograms of S1-600 and S2-600 show reflections ascribed to additional $\text{Li}_2\text{MnSiO}_4$ polymorphs. Sample S1-600 displays a peak at $2\theta = 30.6^\circ$ (031), indicating the formation of the $Pmnb$ polymorph of $\text{Li}_2\text{MnSiO}_4$; in contrast, for sample S2-600, the additional peak at $2\theta = 30.2^\circ$ (031) can be ascribed to the $P2_1/n$ polymorph.^[2,16] These polymorphs are commonly obtained at higher temperatures. The $P2_1/n$ polymorph of $\text{Li}_2\text{MnSiO}_4$ has only been reported to occur at temperatures typically above 900 °C. The formation of these polymorphs at the relatively low calcination temperature of 600 °C may be attributed to the formation of a Li-rich phase $\text{Li}_{2+2x}\text{Mn}_{1-x}\text{SiO}_4$ ($0 < x < 1$), as assumed for the samples calcined at 900 °C. Refinement was carried out using modified structural models of γ_{II} - $Pmnb$ and β_{II} - $Pmn2_1$ to determine the presence of a mixture of $\text{Li}_2\text{MnSiO}_4$ polymorphs in samples S1-600 and S2-600.^[2,18] The Li–Mn anti-site defect was considered for the γ_{II} - $Pmnb$ model, which is reported to be the most favorable intrinsic disorder of $\text{Li}_2\text{MnSiO}_4$.^[20] Migration of Li, Mn, and Si atoms to alternative tetrahedral sites in the hexagonal-close-packed (HCP) array of oxygen atoms was not taken into account for the β_{II} - $Pmn2_1$ model. Moreover, the Li and Mn content was not confined to 2 and 1, respectively, to determine the Li/Mn cation ratio of the $\text{Li}_2\text{MnSiO}_4$ structure. The refinement results indicate that for both samples S1-600 and S2-600, two phases ($\beta + \gamma$) are formed along with the MnO by-product, as observed for samples S1-900 and S2-900. The β -phase of sample S1-600 was indexed as $Pmn2_1$ with a calculated Li/Mn cation ratio of 2.01:0.99. The Li-rich γ -phase is of space group (s.g.) $Pmnb$ with a calculated Li/Mn cation ratio of 2.39:0.61. Accordingly, sample S2-600 was fitted to binary phases of $\text{Li}_2\text{MnSiO}_4$. The Li/Mn cation ratios of the β and γ phases are 2.00:1.00 and 2.25:0.75, respectively. The γ -phase of S2-600 was s.g. $P2_1/n$, which differs to the γ -phase of S1-600. The reasons for this are currently unclear but could be attributed to the Li amount in solid solution, which is calculated to be higher in the $Pmnb$ structure.

To obtain a further understanding of sample S2-600, TEM studies were performed. An overview image is shown in Figure 5a where an agglomeration of nanosized particles is shown. Obtaining high-resolution (HR)-TEM information is chal-

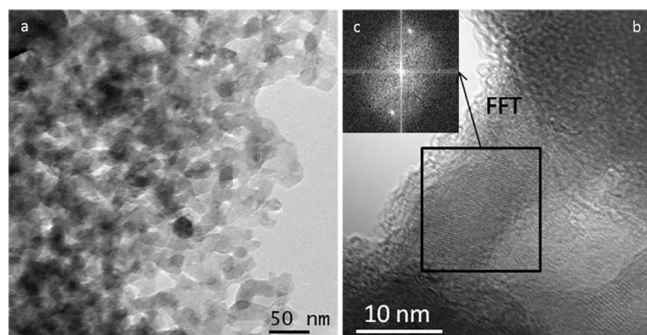


Figure 5. TEM images of S2-600: a) Overview image of an agglomeration of nanosized particles; b) HR-TEM image; c) FFT of the selected area (black square) with lattice plane distance of 0.294(2) nm, corresponding to (031) plane of the $P2_1/n$ phase of $\text{Li}_2\text{MnSiO}_4$.

lenging for this material due to the high electron beam sensitivity, polymorphic (orthorhombic and/or monoclinic) structure, accompanying non-crystalline material, and small particle size. Figure 5 b shows a HR-TEM image that partially presents lattice planes of a small particle. The corresponding fast Fourier-transform (FFT, inset c in Figure 5) delivers an experimental lattice plane distance of 0.294(2) nm, which agrees with the lattice plane distance of 0.295 nm of (031) for the $P2_1/n$ phase of $\text{Li}_2\text{MnSiO}_4$ calculated from the crystallographic data and JEMS software of Piere Stadelmann.^[14] Additionally on the same sample, electron energy loss spectroscopy (EELS) was performed. Solely the expected elements for $\text{Li}_2\text{MnSiO}_4$ were detected. The obtained spectra are shown in Figure 6. All spectra show power-law background-corrected raw data. The near edge structure of the Si-L_{2,3} edge presents a small peak at 105.7 eV, a sharp peak at 107.7 eV, and a broad peak at 114 eV

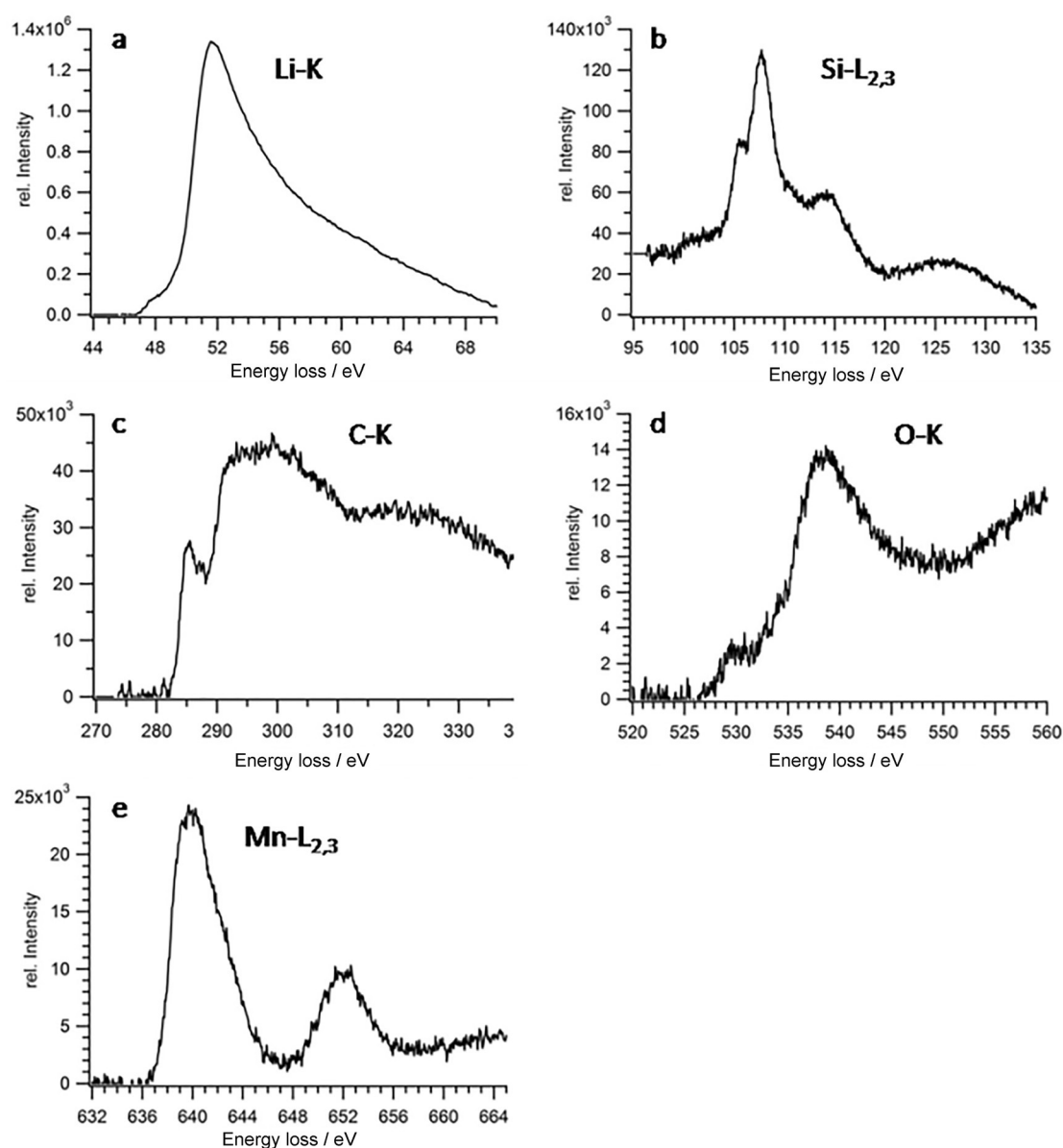


Figure 6. Electron-energy-loss spectra of S2-600: a) Li-K edge, b) Si-L_{2,3} edge, c) C-K edge, d) O-K edge, and e) Mn-L_{2,3} edge.

energy loss. These peak positions and shapes correspond to those reported for Si located in a SiO_4 tetrahedron.^[30] The C-K edge presents a characteristic near-edge structure for amorphous carbon with a π^* peak at 285 eV and a broad σ^* peak starting at 293 eV energy loss.^[30,31] The near-edge structure of the oxygen edge correlates with those known from FeO with a shoulder starting at 529 eV and a narrow peak with a maximum at 536.6 eV.^[32] The Mn $L_{2,3}$ edge shows the separated L_3 and L_2 peaks located at an energy loss of 640 eV for the L_3 edge and 652 eV for the L_2 edge, where the maximum of the L_3 edge at an energy loss of 640 eV can be correlated to the presence of mainly Mn^{2+} in a high spin state.^[30] All the near-edge structure correlation of the Si, C, O, and Mn edges fulfill the expectation for the $\text{Li}_2\text{MnSiO}_4$ phase with additional amorphous carbon. In good agreement with XRD findings, these results confirm the presence of the $P2_1/n$ polymorph of $\text{Li}_2\text{MnSiO}_4$ in sample S2-600 and suggest that such phases could be formed at relatively low calcination temperatures, that is, 600 °C, for Li-rich solid solutions of $\text{Li}_2\text{MnSiO}_4$.

XRD analysis of samples S3-600, S4-600, S5-600, and S6-600 shows that all crystallize as the $\beta_{\text{II}}\text{-P}m\bar{2}_1$ polymorph of $\text{Li}_2\text{MnSiO}_4$. The sample S3-600 contains the expected MnO by-product. The composition of samples S4-600 and S5-600 located within the triangle $\text{Li}_2\text{SiO}_3\text{-Li}_2\text{MnSiO}_4\text{-Mn}_2\text{SiO}_4$ of the phase diagram are estimated to contain both the Li_2SiO_3 and Mn_2SiO_4 by-products; however, these silicate by-products are either accounted for in small quantities or not present in their crystalline form (see Table 2). A small amount of crystalline Mn_2SiO_4 is identified in XRD measurements of samples S4-600 and S5-600. Unlike the samples calcined at 900 °C, the Li_2SiO_3 and Mn_2SiO_4 phases are possibly present as amorphous solids due to the relatively low calcination temperature applied, and therefore not easily detected by XRD measurements.^[33] Indeed, the diffractograms of samples S5-600 and S6-600 show a single broad diffuse peak at approximately $2\theta = 27^\circ$ that can be ascribed to Li_2SiO_3 in an amorphous state. However, this peak was not observed for sample S4-600 but rather a peak at $2\theta = 30.5^\circ$ (113), which is attributed to crystalline MnSiO_3 (PDF 01-076-0523) but in a very small amount of a few percent. This phase is not predicted to form according to the phase diagram but may occur due to an inhomogeneous mixture of precursors during solid-state synthesis.

Attenuated total reflection infrared spectroscopy (ATR-FTIR) was carried out for all samples calcined at 600 °C to detect possible differences in structure not detectable by XRD measurements. The mid-infrared spectra are shown in Figure 7. In the region 1000–800 cm^{-1} , the stretching vibrations of the Si–O bonds in the $[\text{SiO}_4]^{4-}$ polyanions are represented by many split bands due to the neighboring LiO_4 and MnO_4 tetrahedra.^[34] Asymmetric stretching vibrations at 833 cm^{-1} (ν_1) and 865, 882, and 917 cm^{-1} (ν_3) are observed.^[35] For samples S1-600 and S2-600 that are assumed to be Li-rich solid solutions of $\text{Li}_2\text{MnSiO}_4$, the band at 917 cm^{-1} is shifted to 905 cm^{-1} and an unidentified shoulder at 754 cm^{-1} is observed. The bands observed in the region 600–400 cm^{-1} , that is, 478, 511, and 577 cm^{-1} , are attributed to the bending vibrations (ν_4) of the SiO_4 tetrahedra.^[36] A very weak band at 1088 cm^{-1} is observed

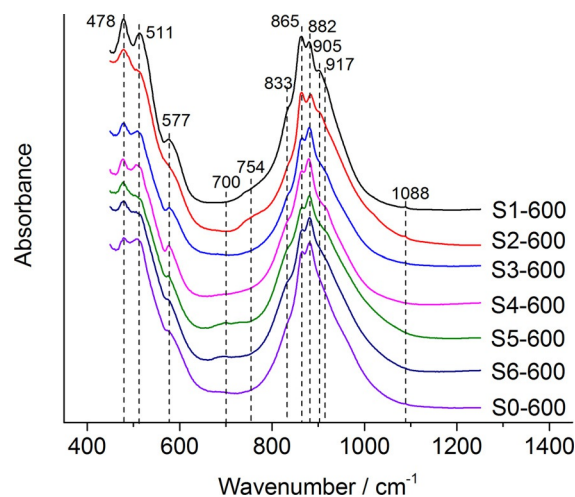


Figure 7. ATR-FTIR absorption spectra of all samples prepared at 600 °C calcination temperature.

for sample S0 and for Li and/or Mn-rich compositions, that is, S1-, S2-, and S3-600. For samples S4-600 and S5-600, a weak band at 700 cm^{-1} may possibly be attributed to the rocking vibrations of the Si–O–Si bridges in Li_2SiO_3 .^[37] According to the ATR-FTIR results, there are differences between the Li-rich samples and samples containing excess Si. Taking a closer look at the lattice parameters determined from the refinement in Table 2 and shown in Figure 8, a dependence can be observed based on the stoichiometric ratio of reactants in the sample. For the samples containing excess Si, the lattice parameter b is larger than 5.39 Å, which is more than the literature value of 5.380 Å.^[2] A near-linear trend can also be observed for b depending on the mol% of Si present in the sample (Figure 8b). The value of the lattice parameter c for samples with approximately stoichiometric $\text{Li}_2\text{MnSiO}_4$ composition, for example, $c = 4.9726$ Å for sample S0-600, are comparable to those found in literature, $c = 4.9662$ Å.^[2] For the Li-rich samples S1-600 and S2-600, an increase in the value of c is observed, from a value of approximately 4.97 Å for the near-stoichiometric $\text{Li}_2\text{MnSiO}_4$

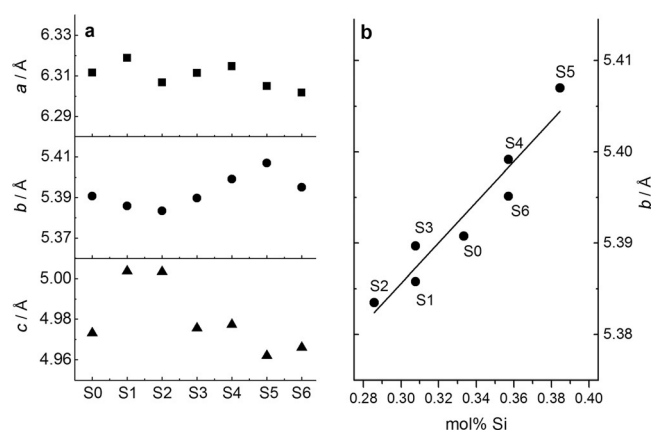


Figure 8. a) Lattice parameters a , b , and c of all samples calcined at 600 °C, b) correlation of the lattice parameter b with the Si content in the sample.

phases to approximately 5.00 Å for the Li-rich $\text{Li}_2\text{MnSiO}_4$ phases. These results indicate a difference in structure due to the composition of the samples.

Electrochemical characterization

The electrochemical behavior of the $\text{C}/\text{Li}_2\text{MnSiO}_4$ samples calcined at 600 °C was investigated by continuous cycling between 1.5 and 4.8 V at C/20 rate assuming a theoretical capacity of 333 mAh g^{-1} . The capacity values are normalized to the overall weight of $\text{Li}_2\text{MnSiO}_4$ as synthesized, which includes the electrochemically inactive secondary phases previously described (Table 2). Figure 9a displays the charge and discharge profiles of the first cycle for all samples. Figure 9b shows the evolution of the discharge capacity over 10 cycles. For the sake of comparison, the samples obtained at 900 °C were electrochemically tested under the same conditions. Figure 10 displays the discharge capacity versus cycle number. As expected, these samples show much lower electrochemical performance than those obtained at 600 °C. In addition, for the set of samples obtained at 900 °C, it is difficult to define a correlation be-

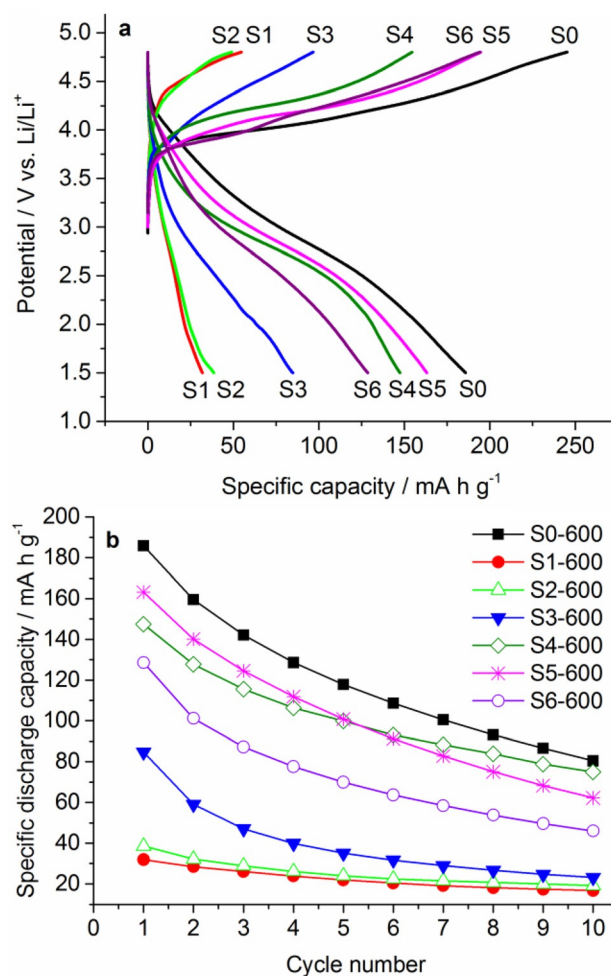


Figure 9. Electrochemical performance of samples obtained at 600 °C calcination temperature: a) first charge and discharge profiles, b) discharge capacity of first ten cycles.

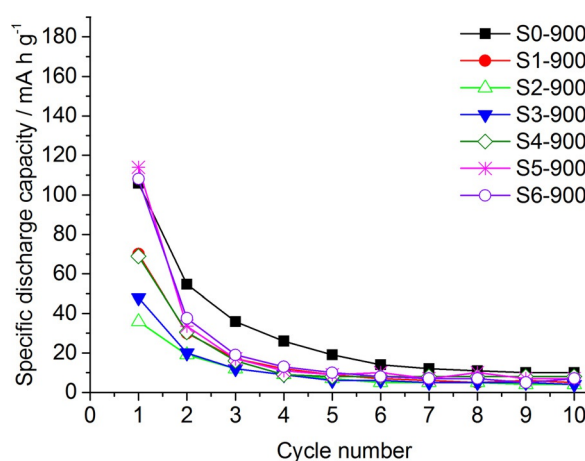


Figure 10. Discharge capacity of first ten cycles of samples obtained at 900 °C calcination temperature.

tween composition and electrochemical results as different factors may have contributed to the poor capacity. As reported in Table 2, these samples have a significantly larger crystallite size than those prepared at 600 °C. Furthermore, the crystallite sizes vary widely amongst the different samples. For example, S1-900 and S2-900 have crystallites larger than 250 nm whereas S6-900 has crystallites of approximately 80 nm. The high calcination temperature leads to crystal growth and the formation of different $\text{Li}_2\text{MnSiO}_4$ polymorphs within the samples. As a consequence, it is not possible to ascribe the difference in the capacity to a single parameter due to the inhomogeneity of the samples obtained at 900 °C. Moreover, these samples contain much less carbon, <2 wt%, which further affects the conductivity and thus the electrochemical performance. On the other hand, all samples calcined at 600 °C have the $Pmn2_1$ polymorph of $\text{Li}_2\text{MnSiO}_4$ as the main phase, a similar carbon content of 5 wt%, and crystallite dimensions of less than 30 nm. Therefore, with the aim of understanding the trend between sample composition and electrochemical results, only samples obtained at 600 °C will be evaluated in this study. As shown in Figure 9a, for all samples a sloped charge and discharge profile is observed and no voltage plateaus can be identified. Flat voltage plateaus are theoretically predicted to occur at approximately 4.4 V for the extraction of the first Li ion and 4.3 V for the extraction of the second Li ion; however, appearance of these flat plateaus have not yet been achieved experimentally, which is attributed to structural collapse due to layer exfoliation upon galvanostatic Li removal from the $\text{Li}_2\text{MnSiO}_4$ framework.^[4] A clear change in capacity based on the composition of the sample is observed. Sample S0-600 consists of phase-pure $Pmn2_1$ - $\text{Li}_2\text{MnSiO}_4$ as determined from XRD measurements and displays the highest specific capacity. A capacity of 245 mAh g^{-1} during the first charge and 186 mAh g^{-1} during subsequent discharge is obtained, corresponding to the extraction/insertion of 1.47 and 1.12 Li ions per formula unit, respectively. The observed capacity is significantly lower than the theoretical value of 333 mAh g^{-1} ; however, only sample S0-600 is able to reversibly exchange more than one Li ion per formula

unit in the first cycle. As commonly observed for $\text{Li}_2\text{MnSiO}_4$ cathodes, the cycling stability is quite poor.^[5] The discharge capacity reduces to 80 mAh g^{-1} , corresponding to 0.48 Li exchanged per formula unit, after 10 cycles.

Samples S4-600 and S5-600 are estimated to contain both the Li_2SiO_3 and Mn_2SiO_4 by-products and the lowest amount of the $\text{Li}_2\text{MnSiO}_4$ phase, corresponding to 62 and 46 wt% composition, respectively. However, these samples demonstrate the highest capacity of all non-stoichiometric samples. The first charge/discharge capacity for sample S4-600 is 154 and 147 mAh g^{-1} , respectively. A small irreversible capacity loss of approximately 5% is observed in the first cycle, which is quite unusual for this material. The first charge and discharge capacity of sample S5-600 is 194 and 163 mAh g^{-1} , respectively. Capacity fading of sample S4-600 is less pronounced than that of sample S5-600. After the fifth cycle, both electrodes show a discharge capacity of approximately 100 mAh g^{-1} . After ten cycles, the discharge capacity obtained for sample S4-600 is similar to that of the sample S0-600, which contains phase-pure $\text{Li}_2\text{MnSiO}_4$. As samples S4-600 and S5-600 show very similar electrochemical behavior, it is possible that indeed a very small amount of impurities are formed. Moreover, the amount of the electrochemically active $\text{Li}_2\text{MnSiO}_4$ phase can be higher than the estimated weight in the actual sample composition. This may be possible due to the low calcination temperature and possible inhomogeneous mixing of the precursors, which represents an intrinsic limitation of solid-state synthetic procedures. Another explanation for the high specific capacity of these two samples is the presence of a secondary phase that facilitates Li exchange, such as a Li ionic conductive matrix. A study has shown that the Li_2SiO_3 by-product, in the form of an ionic conductive matrix surrounding the electrochemically active $\text{Li}_2\text{FeSiO}_4$ phase ($0.8\text{Li}_2\text{FeSiO}_4/0.4\text{Li}_2\text{SiO}_3$), is beneficial for the overall electrochemical performance through promotion of Li^+ conduction.^[33] However, sample S6-600 expected to have only Li_2SiO_3 as by-product shows a limited discharge capacity with respect to samples S4-600 and S5-600. Indeed, S6-600 shows a first charge capacity as high as sample S5-600 but much higher irreversible capacity loss. The first discharge capacity of S6-600 is limited to 129 mAh g^{-1} . According to these results, the Li_2SiO_3 by-product is either present as an amorphous phase in small quantity or is not able to effectively improve the electrochemical behavior of $\text{Li}_2\text{MnSiO}_4$ -based electrodes.

The poorest electrochemical performance is observed for the samples containing the MnO impurity. MnO is an electrochemically inert phase as observed from ex situ XRD measurements.^[8] However, the amount of MnO in the samples, such as in S3-600, is not enough to justify the loss of capacity due to only inactive material weight. Therefore, the MnO impurity is assumed to alter the conductivity, resulting in low capacities.^[6,29] Samples S1-600 and S2-600 show very similar electrochemical behavior, with the lowest specific discharge capacity of less than 40 mAh g^{-1} . The reduced capacity can be due to many factors. The composition of these samples lies in the region of the phase diagram where Li-rich $\text{Li}_{2+2x}\text{Mn}_{1-x}\text{SiO}_4$ ($0 < x < 1$) solid solutions are assumed to form.

Due to the formation of Li-rich phases, the crystal size of samples S1-600 and S2-600 is two- to threefold larger than samples containing near-to stoichiometric $\text{Li}_2\text{MnSiO}_4$, negatively affecting the electrochemical performance. However, other effects can contribute to capacity reduction. In the case of a Li-rich solid solution, the amount of the transition metal Mn in the structure is reduced, that is, the amount of electrons per formula unit available for the electrochemical reaction is reduced from 2 to 1.5 (assuming the amount of Mn per formula unit is 0.75). Moreover, the presence of different $\text{Li}_2\text{MnSiO}_4$ polymorphs could also have an impact on the overall electrochemical performance. Atomistic simulations of $\text{Li}_2\text{MnSiO}_4$ show that the complexity of migration pathways for Li ions are different depending on the polymorph, the $P2_1/n$ phase being the most complex followed by $Pmnb$ and $Pmn2_1$.^[17] Experimentally it has been shown that the electrochemical performance of the $P2_1/n$ and $Pmnb$ polymorphs of $\text{Li}_2\text{MnSiO}_4$ is worse than that of $Pmn2_1$.^[18,38] Although in the present study a Li excess of 25 mol% is present, Li-rich phases, namely $Pmnb$ and $P2_1/n$, are expected to form even with lower amounts of Li, that is, approximately 10%, as observed for similar structures.^[27,28] However, we cannot exclude different effects on electrochemical behavior of $\text{Li}_2\text{MnSiO}_4$ when a very small amount of Li excess, lower than 10%, is used.

The specific surface area depends on the sample composition, which could also affect the electrochemical behavior. According to Brunauer–Emmett–Teller (BET) measurements, sample S0-600 has the highest surface area of $82.4 \text{ m}^2 \text{ g}^{-1}$. The Li-rich samples S1-600 and S2-600 have the lowest surface area of 47.9 and $20.3 \text{ m}^2 \text{ g}^{-1}$, respectively. Sample S3-600, containing near-stoichiometric $\text{Li}_2\text{MnSiO}_4$ and the MnO impurity, has a surface area of $67.2 \text{ m}^2 \text{ g}^{-1}$. The Si-rich samples S4-600, S5-600, and S6-600 have intermediate surface areas, namely 64.1, 59.2, and $57.4 \text{ m}^2 \text{ g}^{-1}$ respectively.

These results suggest that the sample properties in terms of surface area and specific capacity mainly depend on the amount of the $\text{Li}_2\text{MnSiO}_4$ phase present as $Pmn2_1$ polymorph. Besides the possible influence of the formed $\text{Li}_2\text{MnSiO}_4$ polymorph, an increase in crystallite size and decrease in surface area, together with the presence of the MnO by-product, contribute drastically to the reduction in specific capacity.

Conclusions

Nanosized $\text{Li}_2\text{MnSiO}_4$ samples of systematically varied composition, that is, containing excess Li, Mn, and/or Si, were synthesized to determine the effect of impurities on the electrochemical properties. Due to the complex phase diagram of the $\text{Li}_2\text{O–MnO–SiO}_2$ system, obtaining phase-pure $\text{Li}_2\text{MnSiO}_4$ is challenging. A small change in the stoichiometry can result in either a solid solution of $\text{Li}_2\text{MnSiO}_4$, that is, $\text{Li}_{2+2x}\text{Mn}_{1-x}\text{SiO}_4$ (with $-1 \ll x < 1$) or impurities such as MnO, Li_2SiO_3 , and/or Mn_2SiO_4 . A mixture of polymorphs may also be present depending on the heating conditions. For syntheses where relatively low calcination temperatures are applied, amorphous silicate phases such as Li_2SiO_3 may be present but are not detectable using XRD measurements. This implies that reports that

claim phase-pure $\text{Li}_2\text{MnSiO}_4$ based on XRD measurements alone may be inaccurate. From our study, a synthesized $\text{Li}_2\text{MnSiO}_4$ material appeared to be phase pure when a calcination temperature of 600°C was applied; however, an increase in calcination temperature to 900°C revealed a small amount of Li_2SiO_3 as impurity.

From these results, trends in electrochemical performance can be deduced based upon the composition of the samples. Samples of stoichiometric composition with a Li/Mn/Si ratio of 2:1:1 show the best electrochemical performance. Samples containing excess Si result in the formation of Li_2SiO_3 and Mn_2SiO_4 impurities. However, these impurities do not appear to have a significant impact on the electrochemical performance. On the other hand, the presence of excess Li in the investigated range of 25 mol% is found to negatively affect the electrochemical performance. This amount of excess Li leads to the formation of binary phases of $\text{Li}_2\text{MnSiO}_4$, which includes a near-stoichiometric phase ($Pmn2_1$) and a Li-rich solid solution $\text{Li}_{2+2x}\text{Mn}_{1-x}\text{SiO}_4$ ($0 < x < 1$). The Li-rich phases, namely $P2_1/n$ and Pmn , reduce the amount of electrochemically active Mn and therefore the specific capacity. Additionally, an increase in crystal size and reduction of surface area is observed, resulting in decreased electrochemical performance. Moreover, in samples containing excess Li (Li/Mn/Si $> 2:1:1$), Li ions enter the $\text{Li}_2\text{MnSiO}_4$ structure at Mn sites. The available Mn atoms then react to form MnO, of which the presence is shown to drastically reduce the reversible capacity. Certainly, the synthesis method of choice influences all of the factors aforementioned including the impurities formed, crystallite size, and surface area. Therefore, these results identify trends in the synthesis of $\text{Li}_2\text{MnSiO}_4$ and can be applied to optimize alternative synthesis routes to obtain stoichiometric and phase-pure $\text{Li}_2\text{MnSiO}_4$.

Experimental Section

Synthesis of $\text{Li}_2\text{MnSiO}_4$ samples. $\text{Li}_2\text{MnSiO}_4$ samples were prepared by solid-state reaction based on the work reported by Peng et al. using high-purity reagents $\text{LiOH}\cdot\text{H}_2\text{O}$, $\text{Mn}(\text{CH}_3\text{COO})_2$, and $\text{Si}(\text{OC}_2\text{H}_5)_4$.^[22] All reactants were purchased from Sigma-Aldrich and used as received. The molar ratio of Li/Mn/Si was varied according to Table 1 to obtain powders of various compositions within the ternary Li_2O – MnO – SiO_2 phase diagram. Ethanol and polyethylene glycol were added as dispersing agents. The materials were ball-milled for 6 h at a speed of 450 rpm. The slurry was dried in a vacuum oven at 90°C overnight. The dried material was ground using mortar and pestle. For each sample, the obtained $\text{Li}_2\text{MnSiO}_4$ precursor was fractioned and heated under nitrogen atmosphere at a rate of $5^\circ\text{C}\text{min}^{-1}$ to either 600 or 900°C and held for 15 h. The obtained powders were then slowly cooled to room temperature. The samples were named according to the calcination temperature applied, for example, S0–600 is sample S0 calcined at 600°C .

Structural and morphological characterization. X-ray diffraction (XRD) measurements were performed using a Siemens/Bruker D5000 diffractometer with CuK_α radiation ($\lambda = 0.154$ nm). The diffraction data were collected in the 2θ range between 10° and 120° in steps of 0.04° and a dwell time of 10 s per step. Phase determination was carried out using the Bruker phase analysis software

DIFFRAC.EVA and ICDD PDF-2 Database. Structural information and quantitative phase analysis were determined by Rietveld refinement using TOPAS 4.2 software from Bruker AXS. The morphology of the samples was recorded using a scanning electron microscope (SEM), Zeiss model LEO Gemini 1530 VP. High-resolution transmission electron microscopy (HR-TEM) and electron energy-loss spectroscopy (EELS) were carried out using an objective lens Cs-corrected FEI-TITAN 80–300 equipped with a GIF Quantum 965 energy filter operated at 80 kV to avoid knock-on damage and increase the energy resolution. The electron energy loss data were acquired using the dual EELS mode to correct the energy drift during data acquisition, with a dispersion of 0.05 eV per pixel, integrating ten frames with recording times of 0.05 s up to 5 s for sufficient signal-to-noise ratios. The image and EELS data processing were performed using Digital Micrograph (Gatan), JEMS (Piere Stadelmann), and Igor (Wave Metrics) software. All recorded spectra and images were gain- and dark count-corrected. FTIR absorption spectra were recorded using a Bruker Vertex 70 instrument using a Platinum ATR in the wavenumber range of 1250 – 450 cm^{-1} at a spectral resolution of 2 cm^{-1} . The specific surface area was measured using N_2 absorption, BET method on a Thermo Fisher Scientific Sorptomatic instrument. Carbon content of the synthesized $\text{Li}_2\text{MnSiO}_4$ samples was determined using an analytisch multi EA 4000 elemental analyzer.

Electrochemical characterization. Electrodes were prepared from a slurry of 70 wt% $\text{Li}_2\text{MnSiO}_4$ -based powder as active material, 20 wt% Super P Li carbon black (Timcal) and 10 wt% polyvinylidene fluoride binder (Solvay) dissolved in *N*-methyl-2-pyrrolidone (Sigma-Aldrich). The slurry was coated onto an Al-foil current collector using the doctor-blade technique. Circular electrodes of 1.13 cm^2 were punched from the foil, pressed to improve contact between active material, conductive carbon, and current collector, and dried at 120°C under vacuum overnight. The active material loading for all obtained electrodes was 2.6 mgcm^{-2} . T-cells were assembled in an argon-filled glovebox and consisted of the working electrode described above, Li metal as counter and reference electrode, glass microfiber GF/A (Whatman) as separator, and 1 M LiPF_6 in ethylene carbonate/dimethyl carbonate (EC/DMC) 1:1 w/w (battery-grade, Ube Industries) as electrolyte. Cells were galvanostatically cycled at room temperature between 1.5 and 4.8 V at a current corresponding to C/20 using a BaSyTec electrochemical workstation. The current rate was calculated assuming $1\text{C} = 333$ mAhg^{-1} . Three cells were assembled and cycled for each experiment to verify the reproducibility of the results. All potentials are provided in V versus Li/Li⁺.

Acknowledgements

This work was supported by the German Federal Ministry of Education and Research (BMBF) in the project Li-EcoSafe (03X4636 A). The authors would like to thank Gisela Arnold (ZSW), Paul Drews (ZSW), and Claudia Pfeifer (ZSW) for characterization support.

Keywords: electrochemistry • energy conversion • lithium • manganese • silicates

[1] A. Nyttén, A. Abouimrane, M. Armand, T. Gustafsson, J. Thomas, *Electrochem. Commun.* **2005**, *7*, 156–160.

[2] R. Dominko, M. Bele, M. Gaberscek, A. Meden, M. Remskar, J. Jamnik, *Electrochem. Commun.* **2006**, *8*, 217–222.

- [3] M. E. Arroyo-de Dompablo, M. Armand, J. M. Tarascon, U. Amador, *Electrochem. Commun.* **2006**, *8*, 1292–1298.
- [4] H. Lee, S.-D. Park, J. Moon, H. Lee, K. Cho, M. Cho, S. Y. Kim, *Chem. Mater.* **2014**, *26*, 3896–3899.
- [5] R. J. Gummow, Y. He, *J. Power Sources* **2014**, *253*, 315–331.
- [6] A. Kokalj, R. Dominko, G. Mali, A. Meden, M. Gaberscek, J. Jamnik, *Chem. Mater.* **2007**, *19*, 3633–3640.
- [7] M. M. Kalantarian, S. Asgari, P. Mustarelli, *J. Mater. Chem. A* **2013**, *1*, 2847–2855.
- [8] R. Dominko, M. Bele, A. Kokalj, M. Gaberscek, J. Jamnik, *J. Power Sources* **2007**, *174*, 457–461.
- [9] M. Mancini, E. Bekaert, T. Diemant, M. Marinaro, L. de Biasi, R. J. Behm, M. Wohlfahrt-Mehrens, *Electrochim. Acta* **2015**, *176*, 679–688.
- [10] D. M. Kempaiah, D. Rangappa, I. Honma, *Chem. Commun.* **2012**, *48*, 2698–2700.
- [11] D. Rangappa, K. D. Murukanahally, T. Tomai, A. Unemoto, I. Honma, *Nano Lett.* **2012**, *12*, 1146–1151.
- [12] M. K. Devaraju, T. Tomai, A. Unemoto, I. Honma, *RSC Adv.* **2013**, *3*, 608–615.
- [13] T. Kawase, H. Yoshitake, *Microporous Mesoporous Mater.* **2012**, *155*, 99–105.
- [14] V. V. Politaev, A. A. Petrenko, V. B. Nalbandyan, B. S. Medvedev, E. S. Shvetsova, *J. Solid State Chem.* **2007**, *180*, 1045–1050.
- [15] A. R. West, F. P. Glasser, *J. Solid State Chem.* **1972**, *4*, 20–28.
- [16] M. E. Arroyo-deDompablo, R. Dominko, J. M. Gallardo-Amores, L. Dupont, G. Mali, H. Ehrenberg, J. Jamnik, E. Moran, *Chem. Mater.* **2008**, *20*, 5574–5584.
- [17] C. A. J. Fisher, N. Kuganathan, M. S. Islam, *J. Mater. Chem. A* **2013**, *1*, 4207–4214.
- [18] R. J. Gummow, N. Sharma, V. K. Peterson, Y. He, *J. Solid State Chem.* **2012**, *188*, 32–37.
- [19] H. Duncan, A. Kondamreddy, P. H. J. Mercier, Y. Le Page, Y. Abu-Lebdeh, M. Couillard, P. S. Whitfield, I. J. Davidson, *Chem. Mater.* **2011**, *23*, 5446–5456.
- [20] N. Kuganathan, M. S. Islam, *Chem. Mater.* **2009**, *21*, 5196–5202.
- [21] R. Dominko, *J. Power Sources* **2008**, *184*, 462–468.
- [22] Z. Peng, H. Miao, H. Yin, C. Xu, W. G. Wang, *Int. J. Electrochem. Sci.* **2013**, *8*, 903–913.
- [23] A. K. Padhi, K. S. Nanjundaswamy, J. B. Goodenough, *J. Electrochem. Soc.* **1997**, *144*, 1188–1194.
- [24] N. Ravet, J. B. Goodenough, S. Besner, M. Simoneau, P. Hovington, M. Armand in *Proceedings of the 196th ECS meeting*, Honolulu, **1999**, Abstr. 127.
- [25] A. Yamada, S. C. Chung, K. Hinokuma, *J. Electrochem. Soc.* **2001**, *148*, A224–A229.
- [26] G. Mali, A. Meden, R. Dominko, *Chem. Commun.* **2010**, *46*, 3306–3308.
- [27] A. R. West, F. P. Glasser, *J. Mater. Sci.* **1970**, *5*, 557–565.
- [28] P. G. Bruce, A. R. West, *Mater. Res. Bull.* **1980**, *15*, 379–385.
- [29] H. Völlenkne, A. Wittmann, H. Nowotny, *Monatsh. Chem.* **1968**, *99*, 1360–1371.
- [30] L. A. J. Garvie, A. J. Craven, R. Brydson, *Am. Mineral.* **1994**, *79*, 411–425.
- [31] O. Stéphan, P. M. Ajayan, C. Colliex, F. Cyrot-Lackmann, E. Sandre, *Phys. Rev. B* **1996**, *53*, 13824–13827.
- [32] C. Colliex, T. Manoubi, C. Ortiz, *Phys. Rev. B* **1991**, *44*, 11402–11411.
- [33] J. Bai, Z. Gong, D. Lv, Y. Li, H. Zou, Y. Yang, *J. Mater. Chem.* **2012**, *22*, 12128–12132.
- [34] K. Zaghbi, A. Ait Salah, N. Ravet, A. Mauger, F. Gendron, C. M. Julien, *J. Power Sources* **2006**, *160*, 1381–1386.
- [35] R. Gummow, G. Han, N. Sharma, Y. He, *Solid State Ionics* **2014**, *259*, 29–39.
- [36] P. Tarte, *Spectrochim. Acta* **1963**, *19*, 25–47.
- [37] M. Handke, M. Nocun in *Progress in Fourier Transform Spectroscopy, Microchim. Acta: Suppl. 14* (Eds.: J. Mink, G. Keresztury, R. Kellner), Springer, Wien, **1997**, pp. 507–510.
- [38] V. Ramar, P. Balaya, *J. Power Sources* **2016**, *306*, 552–558.

Received: July 6, 2016

Revised: August 29, 2016

Published online on October 6, 2016